# Lidar Observations of Sea-Breeze and Land-Breeze Aerosol Structure on the Black Sea

I. KOLEV, O. PARVANOV, AND B. KAPRIELOV

*Institute of Electronics, Bulgarian Academy of Sciences, Sofia, Bulgaria*

E. DONEV AND D. IVANOV

*Department of Meteorology and Geophysics, Faculty of Physics, University of Sofia ''St. Kliment Okhridski,'' Sofia, Bulgaria*

(Manuscript received 5 November 1996, in final form 8 September 1997)

ABSTRACT

This paper describes results of a lidar study of sea-breeze behavior near Akhtopol in the southeastern corner of Bulgaria. The lidar site was a few hundred meters from the western shore of the Black Sea. Analyses are presented of vertical cross sections at different azimuths through the nearshore atmosphere. Three different stages of the sea–land-breeze circulation are discussed: the offshore land-breeze flow, the near-calm period before the onset of a sea breeze, and an onshore sea-breeze flow. The differences in backscatter between the moist, droplet-laden air over the water and the drier air over land with its smaller particles have allowed the characteristic features of the circulations to be identified. Comparisons to simultaneous pilot balloon and surface meteorological observations have supported the interpretations.

## 1. Introduction

Sea-breeze circulations are mesoscale phenomena that have been the subject of both theoretical (Venkatram 1977; Hsu 1986; Athens 1978; Gruning and Batchvarova 1990) and experimental (Singal et al. 1986; Weil et al. 1988) studies in recent years because they are both interesting and important to the fundamental and applied meteorology and to the behavior of atmospheric pollution. Remote monitoring techniques have found an ever-widening application to the study of these effects. Many studies have been carried out using radars and sodars (Aggarwal et al. 1980; Bacci et al. 1984; Weil et al. 1988), and detailed satellite and ground experiments are being planned. Several investigations near the shoreline were also performed by means of lidars (Wakimoto and McElroy 1986; Melfi et al. 1985; Leeum 1986; Uthe 1994). A mobile lidar in combination with conventional means was used in Canada to follow the planetary boundary layer formation (and the pollution spreading, respectively) close to a lake (Hoff et al. 1982). Two experiments in the United States employed airborne lidars. The first (Wakimoto and McElroy 1986) measured the atmospheric pollution above the city of Los Angeles. The second (Melfi et al. 1985) studied the formation of organized convection during cold air propagation over a warm sea surface.

We have conducted several lidar experiments in Bulgaria's Black Sea coastal zone. These include two ecological studies near the cities of Bourgas and Varna, and three scientific research expeditions that investigated atmospheric planetary boundary layer formation processes (Parvanov et al. 1988a; Parvanov et al. 1988b; Kolev et al. 1994a; Kolev et al. 1994b).

Here, we assess how well a lidar can provide a detailed picture of the formation of the sea-breeze circulation, and its evolution through the diurnal cycle, flowing from sea to land during the day and from land to sea during the night. The behavior of the aerosol layers in the coastal zone that are detected by the lidar provides a means of distinguishing between the different stages of the sea-breeze circulation.

## 2. Methods and apparatus

The lidar was operated throughout the 24-h diurnal cycle to provide a series of vertical cross sections of aerosol backscatter in various directions relative to the coastline. Standard meteorological measurements were also collected to provide a basis for interpreting the lidar data. The standard meteorological measurements included near-surface measurements of the horizontal and vertical wind components, the heat and humidity fluxes, the solar radiation, and pilot balloon measurements of the horizontal wind velocity aloft. We have attempted

*Corresponding author address:* Dr. Ivan Kolev, Institute of Electronics, Bulgarian Academy of Sciences 72, Tsarigradsko shosse Blvd., Sofia 1784, Bulgaria.
E-mail: blteam@phys.acad.bg

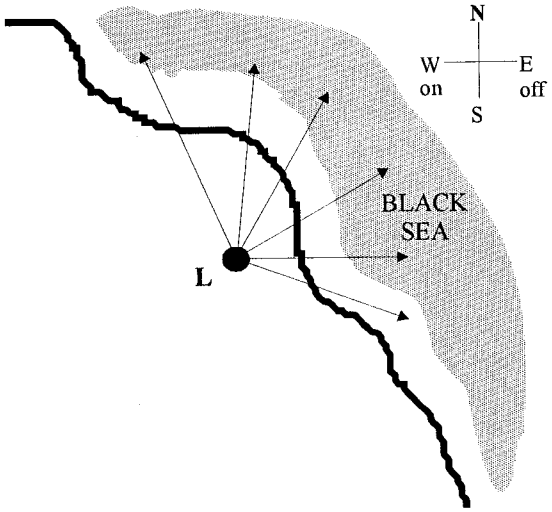


FIG. 1. Map showing the scanning azimuths used during the lidar shoreline experiment; L—location of the lidar; on, off are the onshore and offshore directions, respectively.

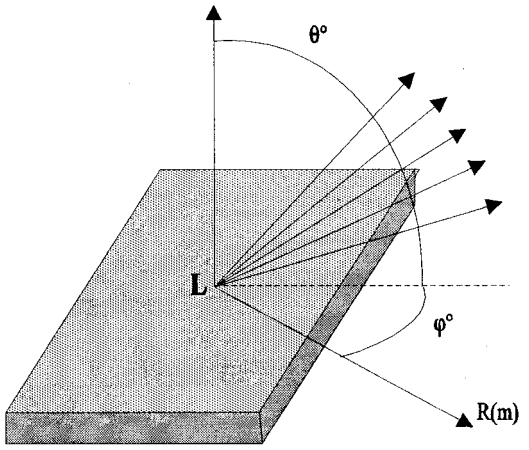


FIG. 2. Schematic diagram of the lidar scanning pattern; $\varphi$ is the azimuthal angle, and $\theta$ is the elevation angle.

to relate the spatial and temporal variations of the aerosol backscattering coefficient with the prevailing atmospheric conditions that could result in the observed variations in optical characteristics of the aerosol. We chose to conduct the experiments where anthropogenic aerosols were practically nonexistant and cloud or fog formation was negligible so that detection of the aerosol movements marking the sea-breeze circulation could be undertaken without confusion or obscuration from clouds.

A scanning aerosol lidar (Kolev 1995) was operated at the Bulgarian Academy of Sciences Institute of Meteorology and Hydrology meteorological station in the eastern part of the Strandzha Mountains, about 5 km southeastward of the town of Akhtopol. The site is about 10 m above sea level and about 200 m from the shoreline. The surrounding land area is characterized by various underlying surfaces, such as cultivated fields, meadows, and forests. The transition from sea to land is abrupt and rocky, with the rocks reaching up to 10 m at some places. Toward the northeast and east, the slope is less steep, about 3°–5° from horizontal. The surrounding hills are about 200 to 300 m above sea level.

The lidar main units are as follows (Kolev et al. 1988, 1995).

- Nd:YAG laser: 532-nm working wavelength, 25-mJ pulse energy, 15–20-ns pulse duration, and adjustable pulse repetition rate of up to 50 Hz;
- receiver: Cassegrainian telescope, 1-m focal length (equivalent), 20-cm diameter;
- photodetector: FEU 84 photomultiplier (PMT) coupled with an interference filter (transmission bandwidth of 1 nm at the working wavelength);
- data acquisition and processing set: HP5180A 10-bit, 20-MHz analog-to-digital converter and PC AT/386 compatible personal computer.

A micrometeorological station measured air and soil temperatures, humidity, horizontal and vertical wind components, total solar radiation, and net radiation (Kolev et al. 1994a). Air temperature and humidity were measured at 1 and 3 m above the surface with Pt 100–type temperature sensors and capacitive polymer humidity sensors. Each pair of temperature and humidity sensors was in a forced ventilation radiation shield. The sensors have sufficiently short lag to allow a scanning period of 1 s. Horizontal wind speed was monitored at 6 m above the ground with a cup anemometer with pulsed output. A sensitive angular motion converter with a resolution of about 0.5° was used so that speeds as low as 5 cm $s^{-1}$ can be measured. Vertical wind was measured with a propeller anemometer and scanned at less than 3-s intervals. Soil temperature was measured at depths of 25, 10, 1, and 0 cm. The pyranometer and net solar radiation monitor were 1.5 m above the surface. The eddy correlation technique was used for direct flux determination.

Two different scanning patterns were used for the lidar observations.

- Horizontal scanning along six azimuths, 336°, 6°, 30°, 60°, 90°, and 110° with respect to north, as shown in Fig. 1.
- Vertical scanning in increments ($\theta°$ in Fig. 2) of 1° between the horizontal and 10° and 2°–5° between 10° and 30°.

The vertical scans provide height–range images (HRI) of the vertical cross section of the aerosol backscattering coefficient field along a fixed azimuth $\varphi$, as shown in Fig. 2. The analyses presented later are based on the vertical scans taken at different azimuths.

The two-dimensional lidar images shown later are grayscale displays of the aerosol backscattering coef-

ficient field. The backscattered light power received by the lidar is related by the lidar equation to the physical properties of the aerosol and its density along the path. The single-scattering approximation of that equation (Collis and Russell 1976) can be written in a slightly modified form as

$$P(r) = E_0 A(c\tau/2) r^{-2} \beta(\pi, r) \exp\left[-2 \int_0^r \alpha(r') r' \, dr'\right], \quad (1)$$

where

| | |
|---|---|
| $P(r)$ | received backscattered light power; |
| $r$ | distance from the lidar; |
| $E_0$ | transmitted laser pulse energy; |
| $A$ | receiver aperture; |
| $c$ | the speed of the light; |
| $\tau$ | duration of the laser pulse; |
| $\beta(\pi, r)$ | aerosol volume backscatter coefficient (steradian$^{-1}$), which is equal to the product of the aerosol volume scattering coefficient and the aerosol backscatter phase function; |
| $\alpha(r)$ | the volume extinction coefficient; |
| $\int_0^r \alpha(r') r' \, dr'$ | the transparency of the atmosphere along the sounding path. |

The volume extinction coefficient $\alpha(r)$ is given by (Hinkley 1976)

$$\alpha(r) = N(r) \int_0^\infty \gamma(a) f(a, r) \, da + \delta(r), \quad (2)$$

where

| | |
|---|---|
| $N(r)$ | number of particles per unit volume at the sounding distance, |
| $a$ | radius of a single particle, |
| $\gamma(a)$ | scattering coefficient for a single particle, |
| $f(a, r)$ | size distribution function of particles, and |
| $\delta(r)$ | volume absorption coefficient. |

At the working wavelength of 532 nm, the contribution of the volume absorption coefficient $\delta(r)$ is negligible. According to Born and Wolf (1968), the Mie scattering of radiation at one wavelength ($\lambda_{\text{fix}}$) by a single spherical particle can be written as

$$\gamma(a) = \pi a^2 k(\rho, n), \quad (3)$$

where

| | |
|---|---|
| $\pi a^2$ | geometrical cross section of the particle, |
| $k(\rho, n)$ | Mie function, scattering efficiency factor, |
| $n$ | complex index of refraction for the particle, and |
| $\rho$ | equals $2\pi a/\lambda_{\text{fix}}$ size of the particle relative to the wavelength. |

The lidar registers the received intensity of the laser radiation backscattered by the aerosol along the sounding path. The above equations provide a most general description of the relations between the microphysical properties of the aerosol, such as size, shape, concentration, and the refractive index and the optical characteristics, such as volume backscattering coefficient and volume extinction coefficient. Obviously, any change in microphysical parameters leads to changes (often considerable) in the optical characteristics. In principle, one could infer the variations taking place in the optical properties of the atmospheric aerosol. However, in practice it is only possible to define qualitative changes in aerosol concentration, providing that the changes in particle size distribution and composition are not too great within the observed volume.

The two-dimensional lidar images were obtained by the following method. Each lidar profile was normalized to remove temporal variations in the energy of the transmitted laser pulses. The received signal was also corrected for the inverse range squared dependence before the natural logarithm was computed.

To reject high frequencies in the lidar profiles, 64 laser shots (for about 2 s) were made in the same direction, and the averaged profile was then stored in the computer. Such filtering eliminates small intensity fluctuations produced by errors in the energy normalization of the individual lidar profiles and high-frequency fluctuations due to PMT noise. The logarithm at every point $S_{ij}$ [which represents one ''point'' of a two-dimensional lidar image (HRI)] of the energy-normalized, range-corrected, and time-averaged lidar profiles (which reflects the aerosol volume backscattering coefficient) is given by

$$S_{ij} = \ln[E_i \beta_i(\pi, r_j)] - 2 \sum_{k=0}^{j} \alpha(r_k), \quad (4)$$

where

| | |
|---|---|
| $r_j = j\Delta$ | distance between the lidar and $j$th scattering range element, |
| $\Delta$ | range increment between successive data points along the sounding path, |
| $i$ | index of the direction of sounding, |
| $j$ | index of the element of the sounding range, and |
| $k$ | summation index. |

The inhomogeneities brought about by the atmospheric turbulence and wind affect the form of the lidar profiles and thereupon the 2D lidar images. Due to the chaotic nature of these inhomogeneities and the magnitude of their intensity, which are comparable in amplitude to the stable aerosol formations, they are capable in blurring the images. The elimination of the influence of such inhomogeneities on the lidar images by means of spatial filters is quite difficult. To reduce the turbulence effects, we average several images repeatedly recorded for a given azimuthal direction. To assess the

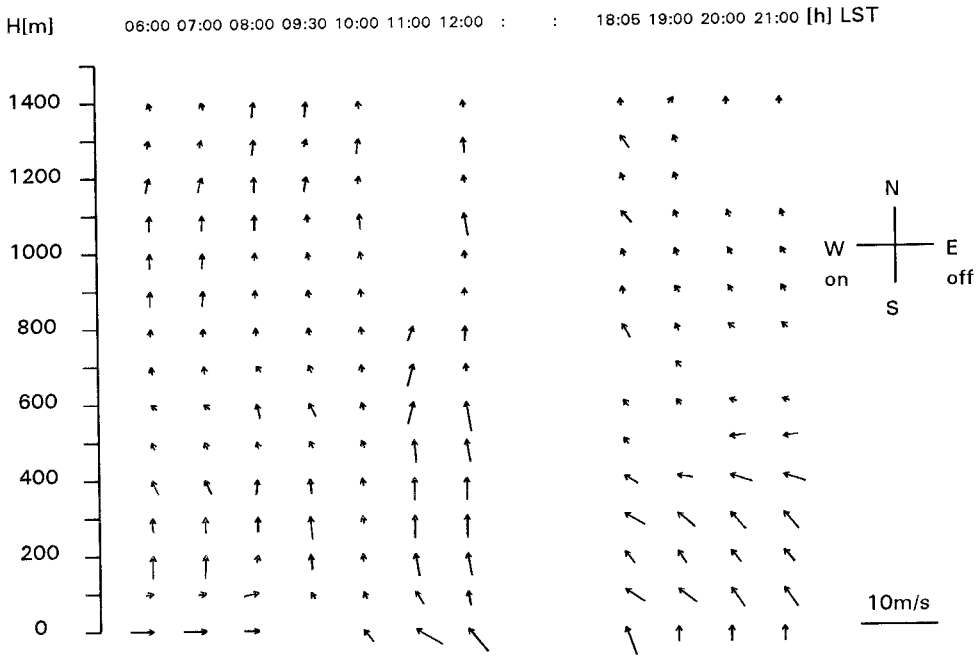


FIG. 3. Pilot balloon wind profiles for 21 June 1993; on, off are the onshore and offshore directions, respectively.

quality of the obtained images, we use a contrast parameter $K$ defined by

$$K_N = \frac{\text{var}\{S_{ij}\}_N}{[\text{mean}\{S_{ij}\}_N]^2}, \tag{5}$$

where $N$ is the number of the averaged images.

Under this procedure uncorrected images, in which objects drifting with the wind velocity are observed, the variance of $S_{ij}$ decreases as $N^{1/2}$, whereas mean $\{S_{ij}\}$ will remain approximately a constant. For example, if the time for a sounding along the $i$th direction is 2 s and 60 such soundings are necessary to obtain 1 HRI, then within a 15-min interval one can average 5–7 HRIs. Thus, if the speed of the wind is 1 m s$^{-1}$ and the size of the turbulent vortices is 500 m, the contrast ($K$) of the inhomogeneities associated with the latter in the averaged image will decrease by a factor of about 2–3.

Another high-reject filtration is performed by running average spatial filter given by

$$F_{ij} = 1/(2n + 1)^2 \sum_{x=-n}^{n} \sum_{y=-n}^{n} S_{i+x,\,j+y}, \tag{6}$$

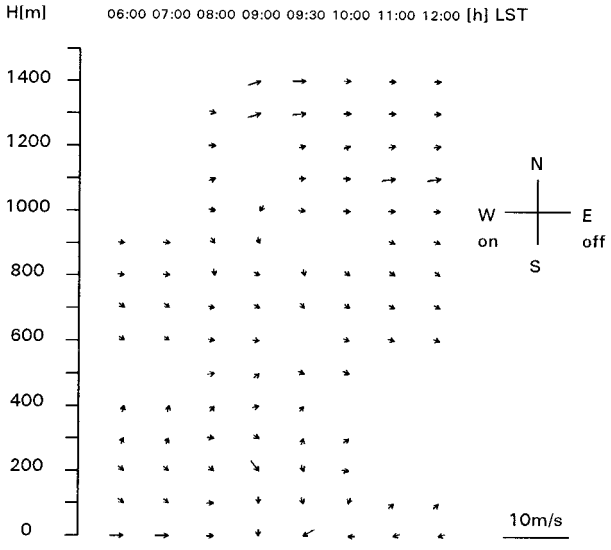


FIG. 4. Pilot balloon wind profiles for 22 June 1993.

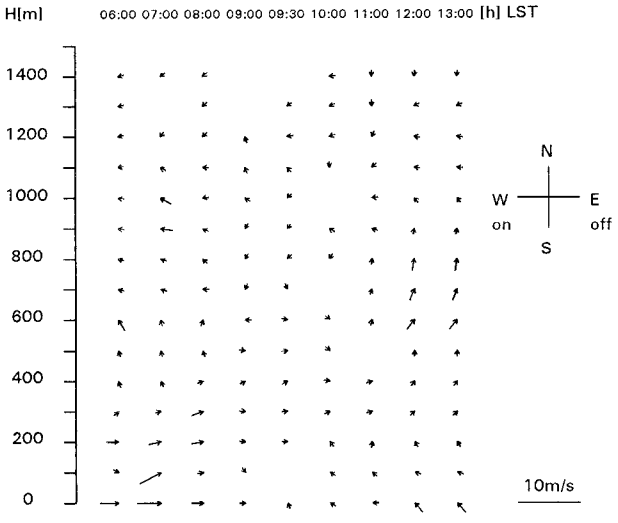


FIG. 5. Pilot balloon wind profiles for 23 June 1993.

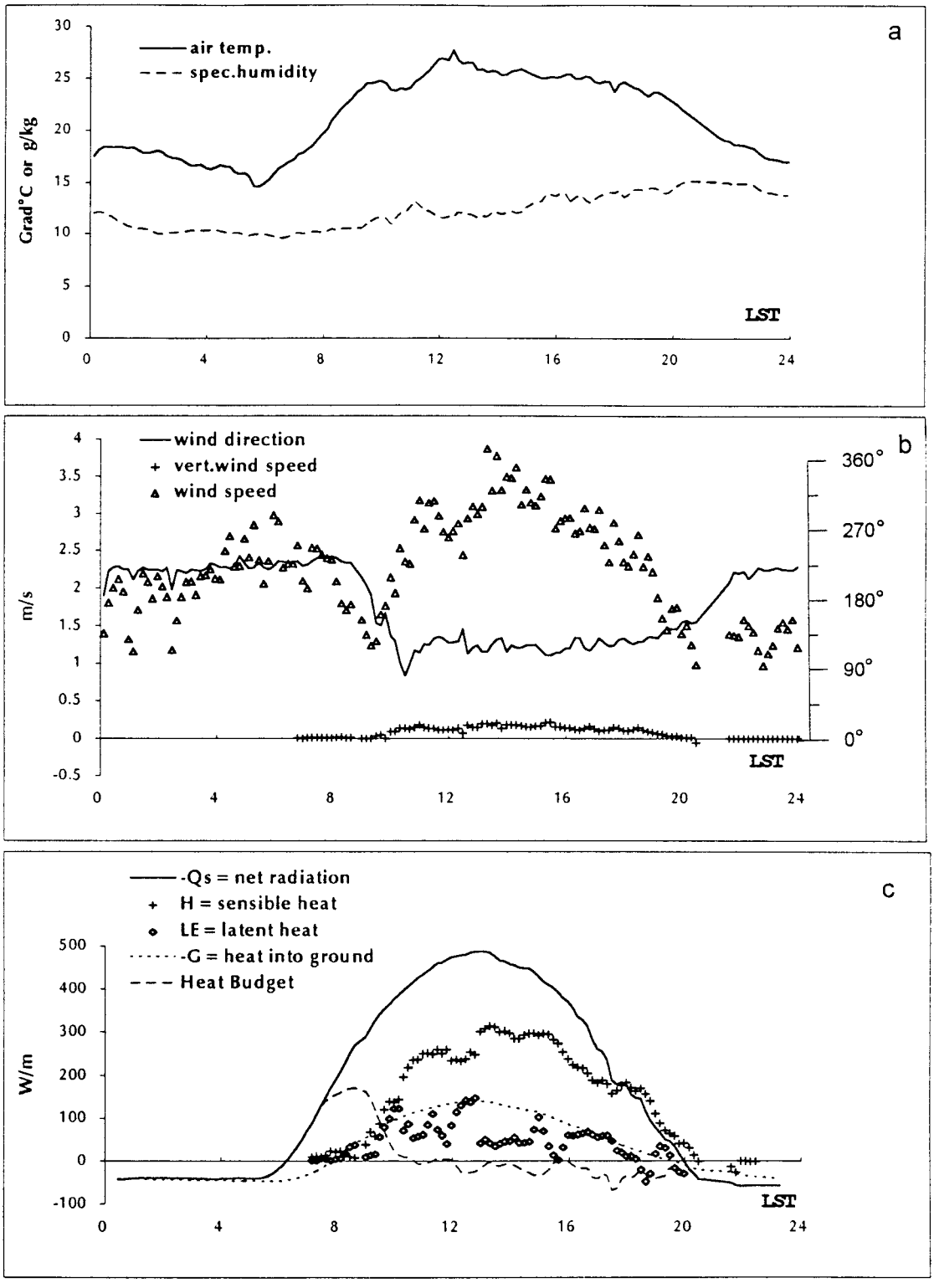


FIG. 6. Meteorological parameters for 21 June 1993.

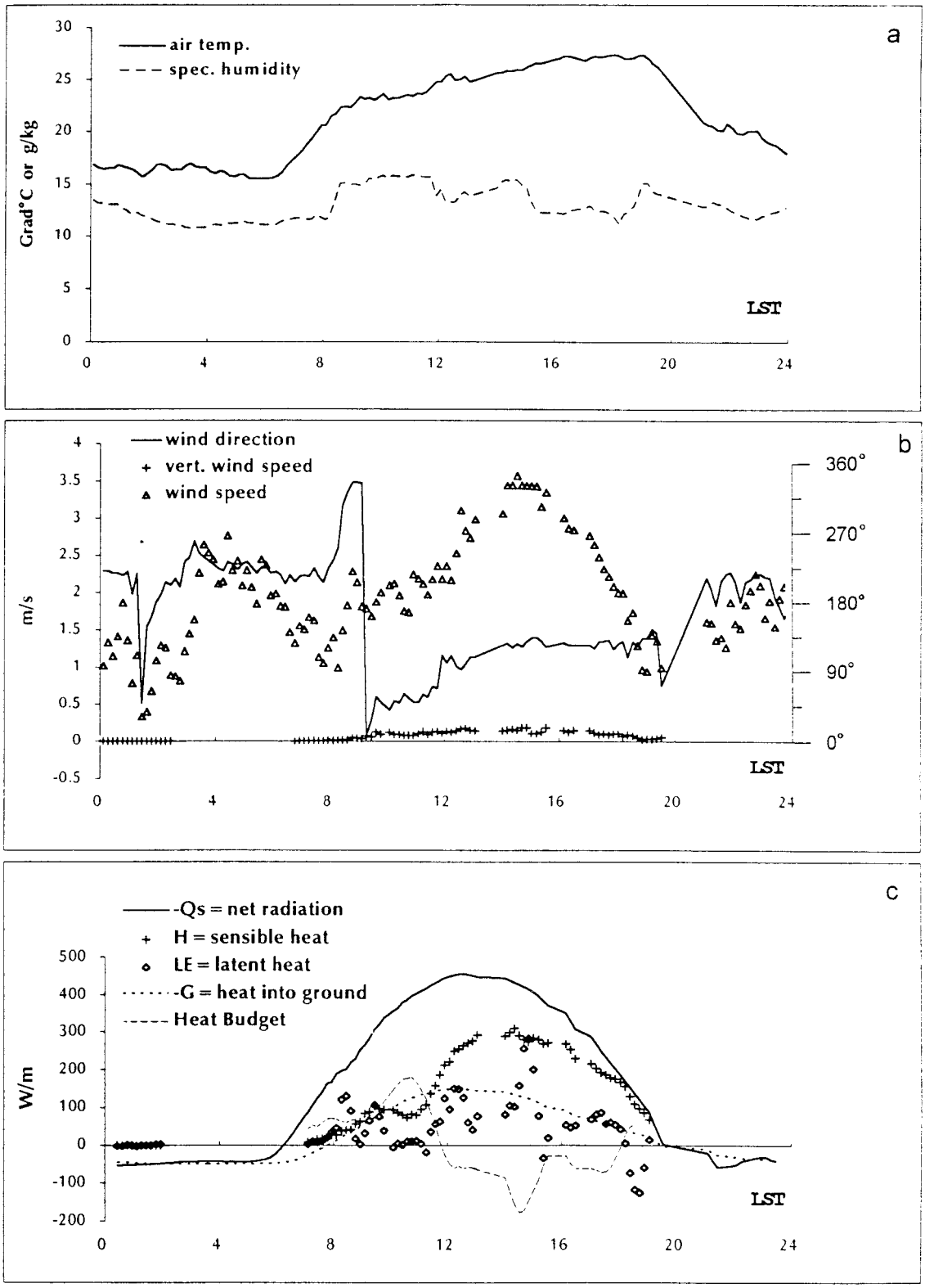


FIG. 7. Meteorological parameters for 22 June 1993.

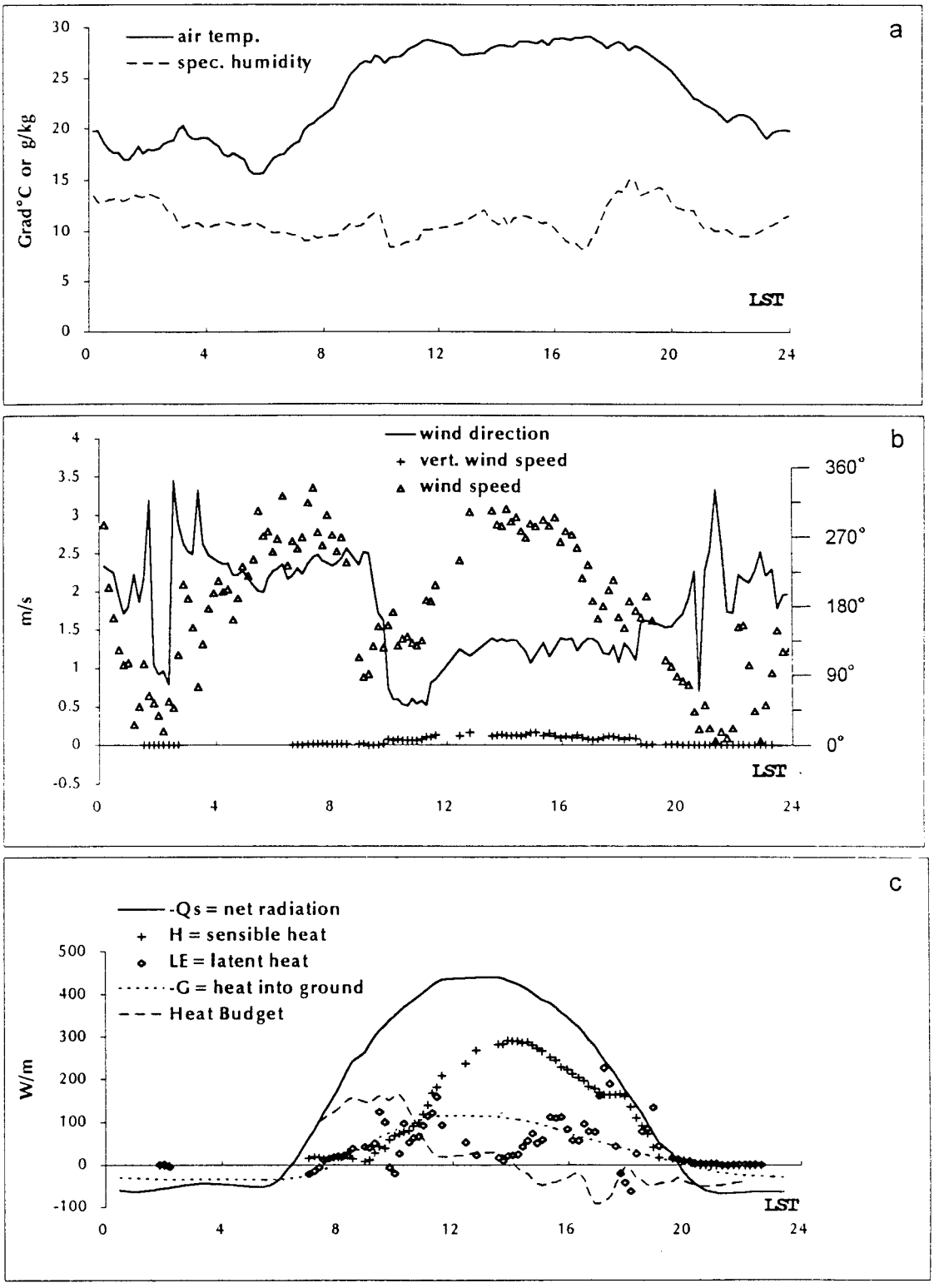


FIG. 8. Meteorological parameters for 23 June 1993.

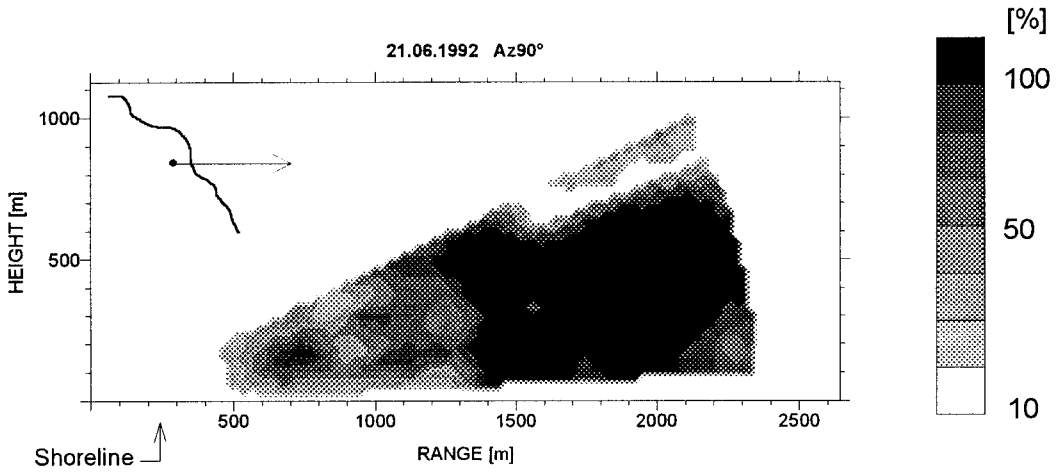


FIG. 9. Lidar vertical cross section at 90° azimuth for land-breeze case, 1902–1917 LST 21 June 1993. In the upper-left corner, the outline of the coast and the azimuthal direction of scanning are shown; the shoreline location along the sounding path is indicated. The vertical cross section of the variations of the aerosol volume backscattering coefficient is presented using eight-degree percentage gray scale.

where 2*n* is the width of the spatial averaging filter. The aerosol inhomogeneities that have a spatial scale of the order of the boundary layer depth typically cause the largest backscatter fluctuations (Kunkel et al. 1980). Since the marine boundary layer depth during the experiments was approximately 1 km, a filter width of 0.05 km is a suitable choice.

## 3. Experimental results

The measurements discussed here were made during the period 18–25 June 1993 (Kolev et al. 1994a,b), mainly on clear days accompanying larger-scale high pressure systems when sea-breeze circulations developed. The presence of such a circulation was established by pilot balloon observations, as shown in Figs. 3, 4, and 5. Observations were made before dawn, during the morning change of wind direction, during the formation of a convective atmospheric boundary layer, and after sunset. Local sunset was at about 2051 LST during the experimental period, but the sun was hidden by the surrounding hills after about 1823 LST. The latter time will be referred to as sunset in the figures and subsequent discussions.

### *a. Measurements of the meteorological parameters*

Figures 6a, 7a, and 8a show the air temperature, specific humidity, and other meteorological parameters for 21, 22, and 23 June 1993. The vertical wind component, the horizontal wind speed, and the wind direction are shown in Figs. 6b, 7b, and 8b; heat fluxes and solar radiation are plotted in Figs. 6c, 7c, and 8c. Vertical profiles of wind speed and direction were obtained during the lidar measurement periods with pilot balloons launched at intervals of 30 or 60 min, and tracked by

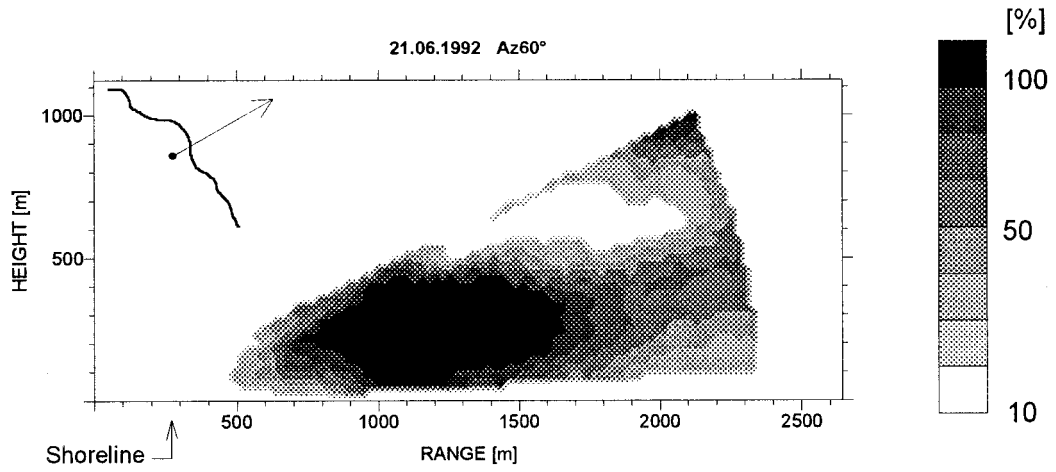


FIG. 10. Lidar vertical cross section at 60° azimuth for land-breeze case, 1923–1939 LST 21 June 1993.

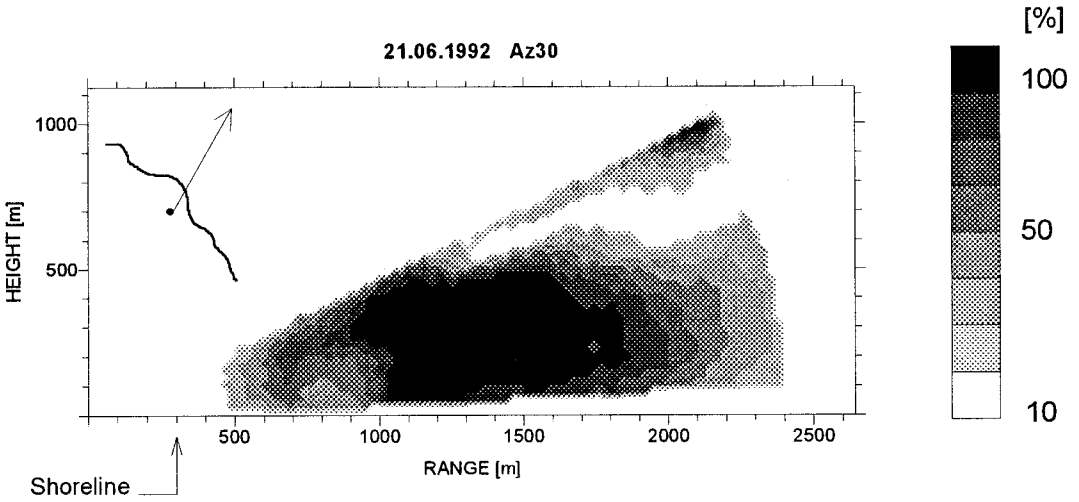


FIG. 11. Lidar vertical cross section at 30° azimuth for land-breeze case, 1943–1958 LST 21 June 1993.

theodolite until they reached altitudes of about 2 km, about 20 min after launch.

### *b. Lidar measurements*

The lidar data are presented as 2D grayscale images representing cross sections of aerosol backscatter in vertical planes. The images can be interpreted qualitatively as relative measures of the aerosol concentration. The cross sections were obtained by both vertical scanning of the atmosphere at different azimuths. Usually, lidar measurements were made for 15 to 25 min out of every 30 min from about 0600 to about 2200 LST to obtain pictures of the backscatter distribution field during different stages of the breeze cycle, namely, land breeze, sea breeze, and the transition periods between them. The lidar maps display the backscatter in vertical planes along different azimuths as grayscale images. The eight levels of gray for each image have been normalized by the maximum observed backscatter for that image.

All the lidar measurements presented here were carried out at a meteorological visibility of greater than 20 km (corresponding to an optical thickness along a sounding path of about 0.2). The good visibility suggests that condensation, and the formation of fog, was not likely to be an important factor. Therefore, most of the observed differences in backscatter are likely due to differences in aerosol concentration or aerosol characteristics associated with differences in humidity. The uniformity of the aerosol might be explained by relatively uniform mixing. Low levels of the turbulence will cause little mixing and are apt to result in large gradients of aerosol density and humidity and hence backscattering.

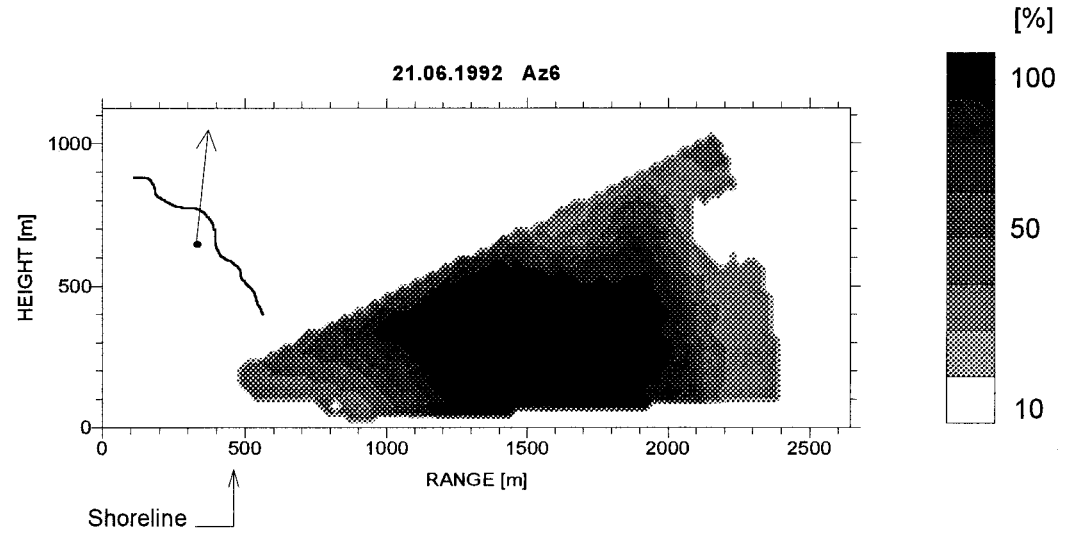


FIG. 12. Lidar vertical cross section at 6° azimuth for land-breeze case, 2002–2019 LST 21 June 1993.

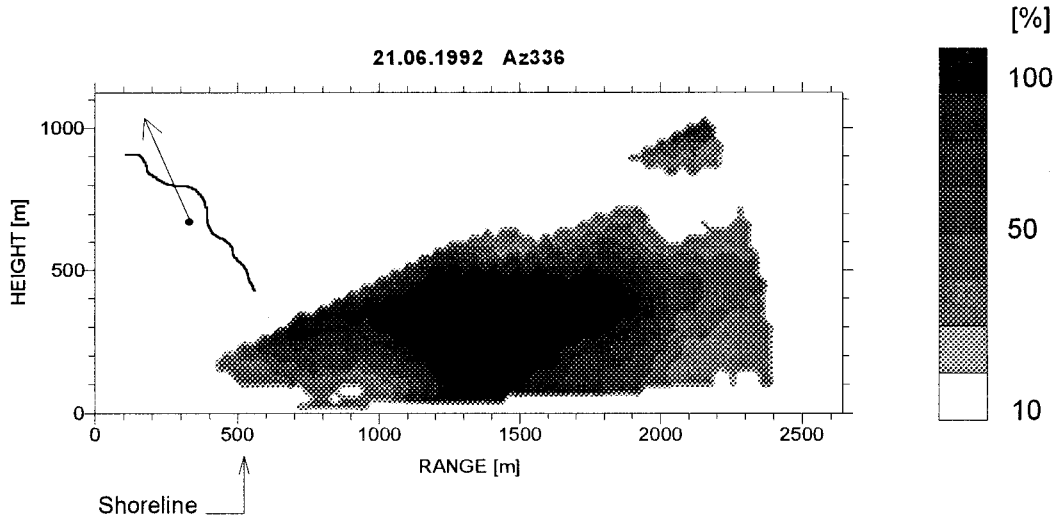


FIG. 13. Lidar vertical cross section at 336° azimuth for land-breeze case, 2024–2042 LST 21 June 1993.

1) LIDAR OBSERVATION OF THE LAND BREEZE

Figures 9–13 show the lidar images at different azimuths between 336° and 90° between 1902 and 2052 LST on the evening of 21 June 1993 in the case of land breeze. They reveal the beginning of a relatively slow night breeze formation after sunset (1823 LST). The seaward advance of the colder and drier air masses from the land carries with it an aerosol with a low-volume backscattering coefficient. The reverse circulation is apparent as the region of relatively high backscattering coefficient that protruded toward the land. The regions at 700–800 m that are relatively free of aerosol are located in a layer of nearly calm winds (see Fig. 3).

The lidar map in Fig. 9 (at 90° azimuth) shows three distinct zones with different aerosol backscatter. The first extends about 250 m to either side of the shoreline; as noted above, this was the region of lowest backscatter coefficient. The second, a transition zone, was located between about 500 and 1300–1400 m from the lidar; it extended to heights of about 500–600 m and separated the region of least backscatter from that with the greatest backscatter. The backscattering coefficient in this transition zone was not uniformly mixed. The final region extended up to about 600-m altitude and about 1000 m beyond the end of the second zone. This is the zone where aerosol backscatter was greatest.

Figure 10 represents the lidar backscatter image along the 60° azimuth. The zone of clear air straddling the shoreline was approximately the same at low altitudes as it is in the 90° azimuth image (Fig. 9), but there appears to have been some clear air penetrating into the transition zone that separated the clearest air from that with the greatest backscatter. This penetration occurred at a distance of about 500–650 m from the lidar. The

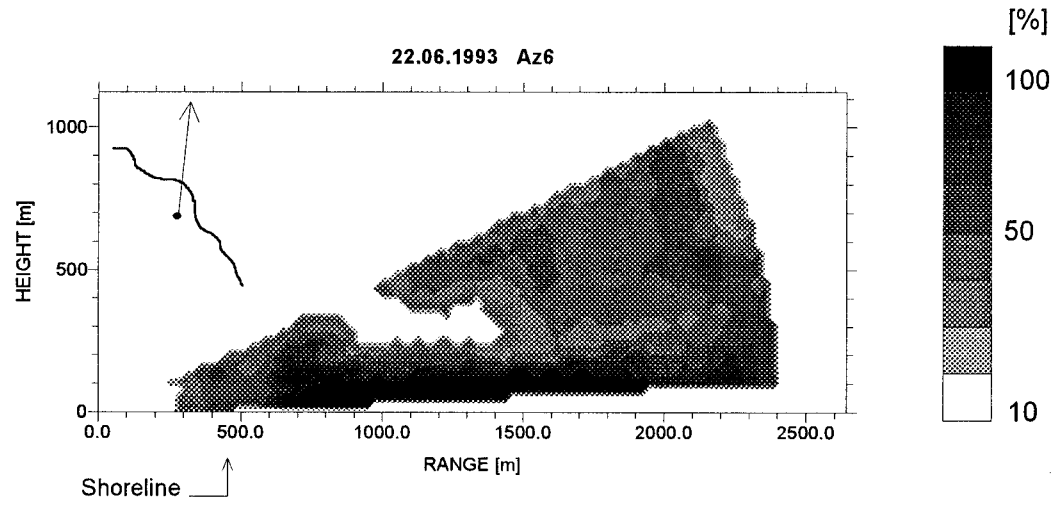


FIG. 14. Lidar vertical cross section at 6° azimuth for sea-breeze case, 0859–0926 LST 22 June 1993.

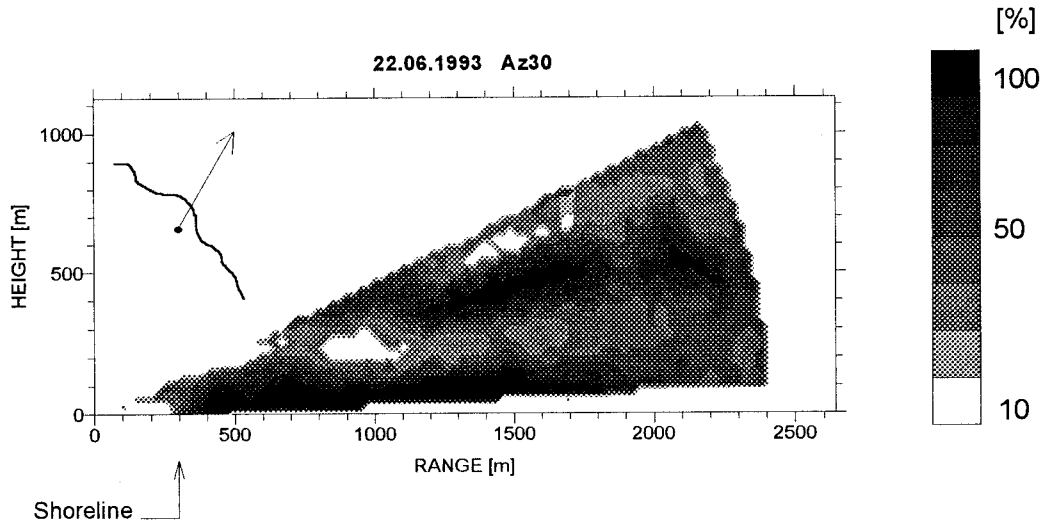


FIG. 15. Lidar vertical cross section at 30° azimuth for sea-breeze case, 0933–0959 LST 22 June 1993.

intermediate zone was considerably narrower than it had been in the easterly direction at the earlier time. The third zone with its high backscatter was also fairly narrow at the surface, extending from about 1000 to about 1300 m from the lidar. The region of greatest backscatter was more extensive aloft—between 700 and 1700 m from the lidar. It appears to have been undercut by the near-surface offshore flow of clearer air, or perhaps the higher backscatter aerosol was being moved toward shore by the return flow aloft.

The 30° azimuth lidar map is given in Fig. 11. The three backscatter zones are still clearly evident. Again, the clearer air extended to about 500 m from the lidar. The transition to higher backscatter took place over the next 500 m, then higher backscatter was observed from about 1000–1800 m. The boundaries between the zones did not change much with altitude up to about 400 m. The image in Fig. 12 is based on data collected about 1 h after those used in Fig. 9. The clearer air appears to have moved offshore with the land breeze in the lowest layers so that it extended to about 900 m from the lidar where the transition zone began. It extended to the beginning of the strong backscatter zone at around 1200 m. Above the surface layer, which only extended to a height of about 100 m, the transition and strong backscatter zones were encountered a few hundred meters closer to the lidar. This geometry is what we might expect if clear air were being advected from shore at the surface, and moister air with larger aerosol particles were moving shoreward in a return circulation aloft. This pattern is even more pronounced in Fig. 13, but this probably reflects the fact that the lidar is pointing in a direction that more nearly parallels the shore. The small region of clear air 900 m from the lidar at the

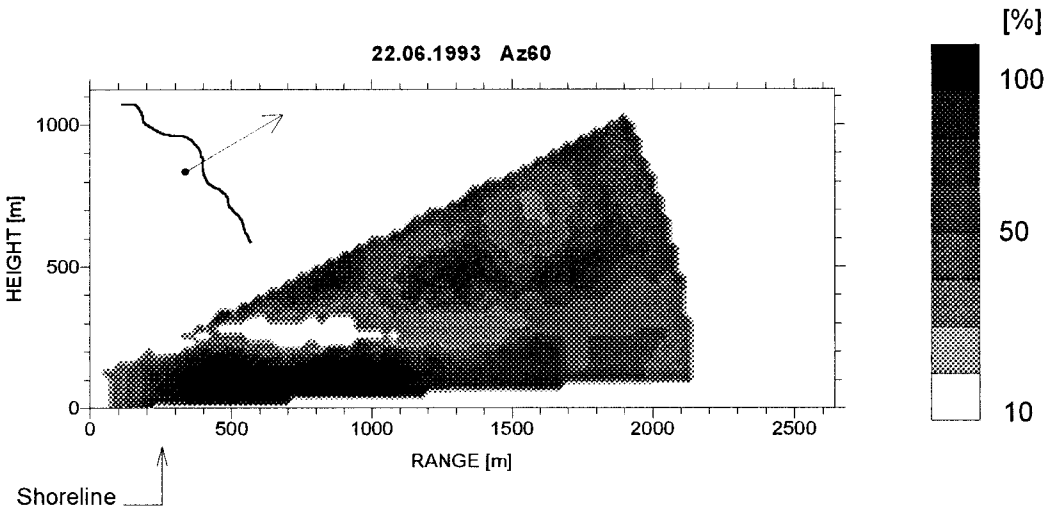


FIG. 16. Lidar vertical cross section at 60° azimuth for sea-breeze case, 0933–0959 LST 22 June 1993.

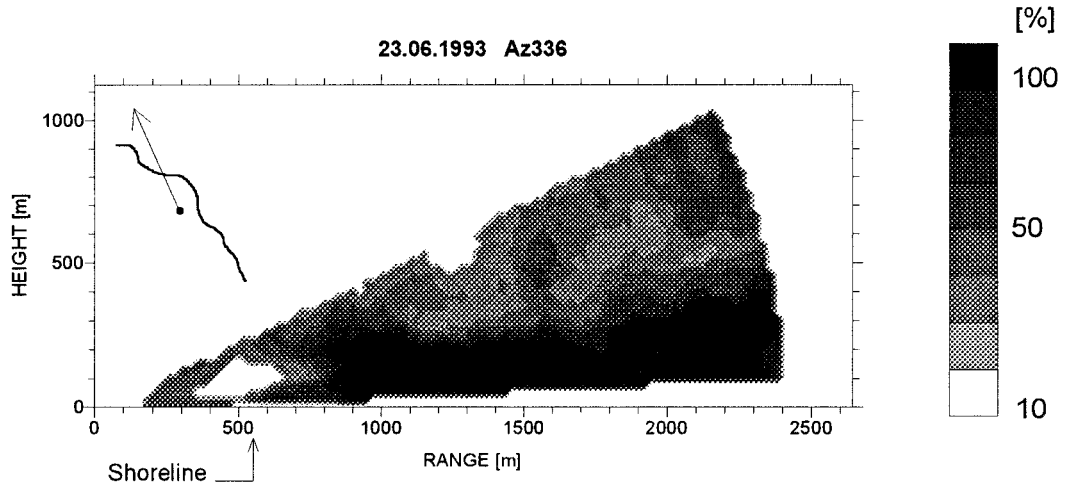


FIG. 17. Lidar vertical cross section at 336° azimuth for calm transition case, 0905–0930 LST 23 June 1993.

surface may be associated with the small point of land that extends toward the cross section there.

The overall picture that emerges from the data displayed in Figs. 9–13 is that there was a shallow layer of clearer air that extended to a height of about 100 m, and outward from the shore about 200 m, where it underwent a transition that caused greater backscatter. The origin of the greater backscatter is not apparent from the lidar observations, but one possibility is that the increased lidar backscatter resulted from increased humidification and aerosol growth as the air moved over the Black Sea. Another possibility is that the increased backscatter is associated with a different air mass, one that has remained over the water for an extended time. The fact that the higher backscatter extends through a deep layer and is advected toward land in the return flow aloft suggests that this is a different air mass that has had time to be modified to higher altitudes. In any event, the lidar has provided a good picture of the land-breeze morphology along the coast.

### 2) LIDAR OBSERVATION OF THE SEA BREEZE

Figures 14–16 show a cross section (at 6°, 30°, and 60° azimuths) of the aerosol structure obtained during the onset of the sea breeze between 0858 and 1037 LST on 22 June 1993. These figures show patterns that are quite different from those of the land-breeze case just discussed. Here, the zone of greatest backscatter was generally confined to the lowest 100 m or so. It appears to be pushing onshore with the flow, while being modified as it progresses over the land. The air in this lowest layer was clearer near the lidar than out over the water. Aloft, at a height of 200–400 m, there was another clear layer that was probably warmer and drier than the air below it. That layer extends seaward. The circulation

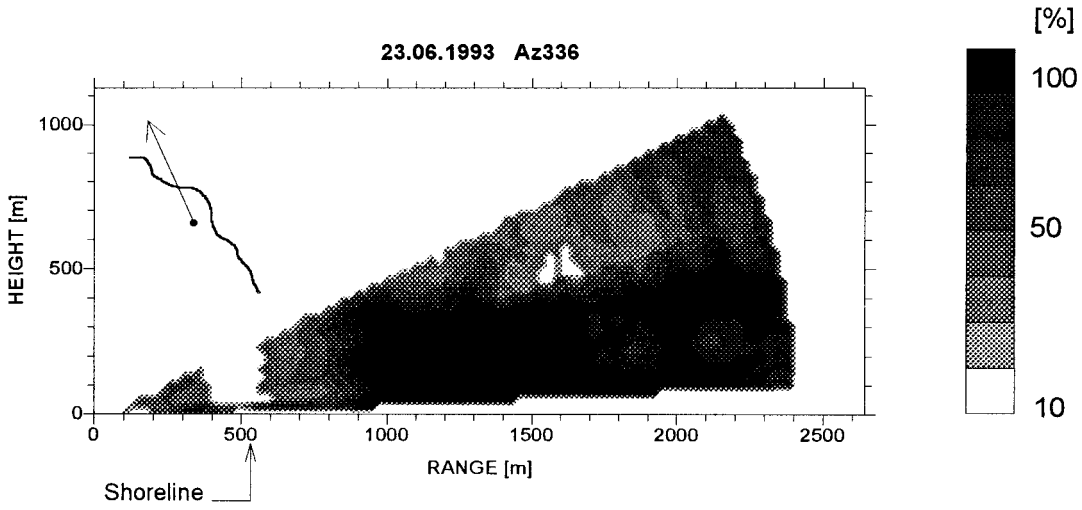


FIG. 18. Lidar vertical cross section at 336° azimuth for calm transition case, 0935–0958 LST 23 June 1993.

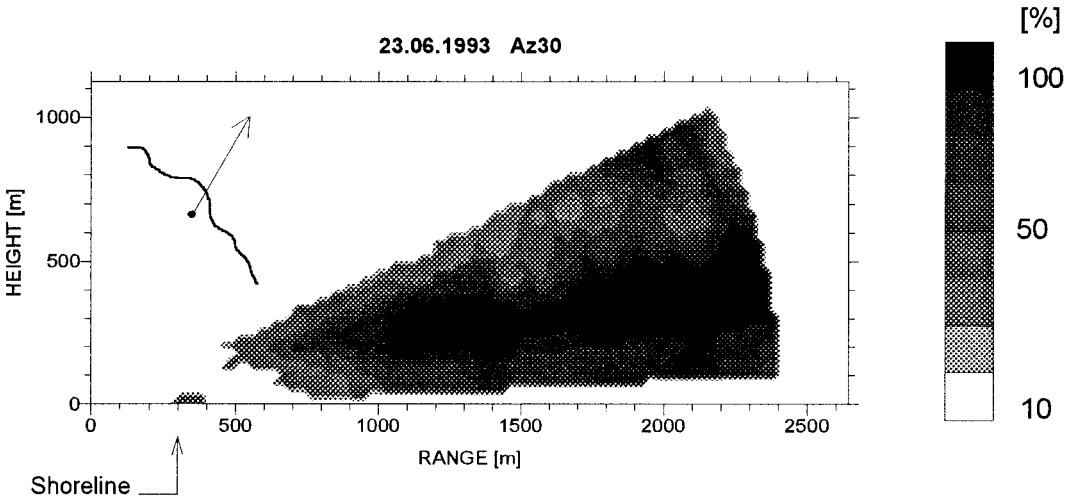


FIG. 19. Lidar vertical cross section at 30° azimuth for calm transition case, 1000–1025 LST 23 June 1993.

that appears to be represented in these figures is, as expected, the opposite of that seen in the land-breeze case. The fact that the layer of greatest backscatter is confined to the lowest part of the atmosphere suggests that little convective mixing has taken place. This in turn suggests that the air was stable because it had been cooled from below.

The meteorological data presented in Figs. 4 and 7 support the above interpretation. An onshore flow began in the layer up to about 100 m above the surface around 0930 LST. At higher altitudes there was a light flow in the offshore direction. Figure 7 shows that the change in surface wind direction is accompanied by an increase in specific humidity, which supports the assumption that the higher backscatter was associated with higher humidity.

#### 3) LIDAR OBSERVATIONS OF THE CALM TRANSITION PERIOD BEFORE THE ONSET OF THE SEA BREEZE

Figures 17–19 show the aerosol backscatter during the morning of 23 June between 0905 and 1025 LST. They show a decrease with time in the aerosol backscattering coefficient over the land; as the day progresses and the air over the land warmed, there was a reduction in the aerosol backscatter. Perhaps the most interesting feature of these cross sections is the column of reduced backscatter at the shoreline. It appears that the sea breeze may have developed over the warm interior before it started along the shore or over the Black Sea. This would have caused a divergence zone near the shoreline at the surface, which in turn would have produced subsidence that brought drier, clearer air down from aloft. The drop in specific humidity at about 1000 LST (Fig. 8) supports this interpretation.

The vertical distribution of backscatter and its evolution with time in Figs. 17 through 19 are different from what we saw in the other datasets. First, there was the column of clear air at the shore mentioned earlier. It formed and appeared to move out over the water, undercutting the layers of stronger backscatter. The greatest backscatter was initially confined to the lowest few hundred meters over the water, but then it moved offshore and deepened. Eventually, a layer of intermediate backscatter was found beneath an elevated layer of greater backscatter. The clearest air appears to have been pushing the other air out to sea at this stage. The picture just described is consistent with a region of subsidence along the shoreline. As the clearer air sinks from aloft, it pushes the more aerosol-laden air away from the shore in both directions. The air pushed away from shore over the land heats and dries so that whatever moist haze might have been present dissipates. The air pushed over the water by the subsidence first appears to have replaced some of the aerosol that was present, perhaps moving under it and lifting it up to a higher level. The replacement air appears to have been humidified and so that the backscatter increased, but not to the backscatter intensities of the air that had been there before.

## 4. Discussion and conclusions

The interpretations presented in the preceding section are based in part on the premise that the optical characteristics of the aerosol reflect certain meteorological conditions, in particular the presence of aerosol and humidity. The dependence of backscatter coefficient on atmospheric humidity has been studied both in laboratory and in field experiments (Covert 1972; Dupont 1994). These studies showed that the backscatter coefficient is considerably affected when the humidity exceeds 60%. It has also been shown by Murayama et al. (1996) that the depolarization of the backscattered laser radiation decreases as the humidity increases. This effect might be useful for some future studies, but it was not

used here. In the analyses presented above, we have used the fact that the backscatter can be used to indicate the origins of the air. Higher backscatter is associated with the moister air over the Black Sea, and clearer air with the drier land conditions. This allowed the motions of the air to be inferred.

The availability of pilot balloon and surface meteorological measurements allowed us to verify the plausibility of the interpretations based on lidar observations alone. These suggest that the lidar data alone can be interpreted to learn a great deal about the nearshore circulations in the lower atmosphere. These lidar data also indicate that some inferences can be drawn about the changes in humidity in the air as it moves from land to sea or vice versa.

*Acknowledgments.* The authors wish to thank Dr. G. Korchev for valuable discussions of the experimental results and R. Nenchev for assistance in the data processing.

## REFERENCES

Aggarwal, S. K., S. P. Singal, R. K. Kapoor, and B. B. Adiga, 1980: A study of atmospheric structures using sodar in relation to land and sea breeze. *Bound.-Layer Meteor.,* **18,** 361–371.

Athens, R. A., 1978: The height of the planetary boundary layer and the production of circulation in a sea breeze model. *J. Atmos. Sci.,* **35,** 1231–1239.

Bacci, P., C. Girand, A. Longetto, and R. Richiardone, 1984: Acoustic sounding of land and sea breezes. *Bound.-Layer Meteor.,* **28,** 187–192.

Born, M., and E. Wolf, 1968: *Principles of Optics.* Pergamon Press, 719 pp.

Collis, R. T. H., and P. B. Russell, 1976: Lidar measurement of particles and gases by elastic backscattering and differential absorption. *Topics in Applied Physics,* Vol. 14, *Laser Monitoring of the Atmosphere,* E. D. Hinkley, Ed., Springer, 71–151.

Covert, D. S., R. J. Charlson, and N. C. Ahlquist, 1972: A study of the relationship of chemical composition and humidity to light scattering by aerosols. *J. Appl. Meteor.,* **11,** 968–976.

Dupont, E., J. Palon, and C. Flamant, 1994: Study of the moist convective boundary-layer structure by backscattering lidar. *Bound.-Layer Meteor.,* **69,** 1–25.

Gruning, S. E., and E. Batchvarova, 1990: Analytical model for the growth of the coastal internal boundary layer during on shore flow. *Quart. J. Roy. Meteor. Sci.,* **116,** 187–203.

Hinkley, E., 1976: *Laser Monitoring of the Atmosphere.* Springer-Verlag, 416 pp.

Hoff, R. M., N. B. A. Trivett, M. M. Millan, P. Fellin, K. G. Anlauf, H. A. Wiebe, and R. Bell, 1982: The Nanticore shoreline diffusion experiment, June 1978, Part III. Ground-based air quality measurements. *Atmos. Environ.,* **16,** 439–454.

Hsu, S. A., 1986: A note on estimating the height of the convective internal boundary layer near shore. *Bound.-Layer Meteor.,* **35,** 311–316.

Kolev, I., 1995: Lidar investigation of the aerosol stratification in the planetary boundary layer (over urban area, mountain valley and coastal zone). *Proc. Workshop on Optical Methods for Environmental Monitoring of the Atmosphere,* Trieste, Italy, NOAA/Environmental Technology Laboratory, 55 pp.

——, O. Parvanov, and B. Kaprielov, 1988: Lidar determination of winds by aerosol inhomogeneities: Motion velocity in the planetary boundary layer. *Appl. Opt.,* **27,** 2524–2531.

——, ——, ——, E. Donev, and D. Ivanov, 1994a: Lidar observation of aerosol stratification in case of sea breeze front. *Proc. 7th ISARS,* Boulder, CO, International Center for Theoretical Physics, 4.9–4.14.

——, ——, ——, ——, and ——, 1994b: Lidar observation of aerosol stratification in the case of sea breeze circulation near the shore. *Comp. Rend. Acad. Bulg. Sci.,* **47,** 21–24.

Kunkel, K. E., E. W. Eloranta, and J. M. Weinman, 1980: Remote determination of winds, turbulence spectra, and energy dissipation rates in the boundary layer from lidar measurements., *J. Atmos. Sci.,* **37,** 978–985.

Leeum, G., 1986: Lidar measurements in the marine atmosphere. *Digest Optical and Millimeter Waves Propagation and Scattering in the Atmosphere,* Florence, Italy, Consiglio Nazionale delle Ricerche, 101–104.

Melfi, S. A., J. D. Spinehirne, S. H. Chou, and S. P. Palm, 1985: Lidar observations of vertically organized convection in the planetary boundary layer over the ocean. *J. Climate Appl. Meteor.,* **24,** 806–821.

Murayama, T., M. Furushima, A. Oda, and N. Tuasakan, 1996: Depolarization ratio measurement in the atmospheric boundary layer by lidar in Tokyo. *J. Meteor. Soc. Japan,* **74,** 571–578.

Parvanov, O., I. Kolev, B. Kaprielov, V. Polianov, and G. Korchev, 1988a: Lidar observation of aerosol structure in the marine planetary boundary layer. *Proc. 14th ILRC,* Innichen-San Candido, Italy, Consiglio Nazionale delle Ricerche and Comitato Nazionale per le Science Fisiche, 49–53.

——, ——, ——, ——, and ——, 1988b: lidar observation of air mass transformation at the sea coast. *Lasers—Physics and Application,* A. Spasov, Ed., Wore Science, 775–781.

Singal, S. P., S. K. Aggarwal, and D. R. Pahwa, 1986: Studies of the marine boundary layer at Tarapur. *Bound.-Layer Meteor.,* **37,** 371–384.

Uthe, E., 1994: Airborne lidar and radiometric detection and analysis of chemical plumes. *Proc. 17th ILRC,* Sendai, Japan, Laser Radar Society of Japan, 40–41.

Venkatram, A., 1977: A model for internal boundary layer development. *Bound.-Layer Meteor.,* **11,** 419–437.

Wakimoto, R. M., and J. L. McElroy, 1986: Lidar observation of elevated pollution layers over Los Angeles. *J. Climate Appl. Meteor.,* **25,** 1583–1599.

Weil, A., and Coauthors, 1988: A mesoscale shear convective cell observed during the C.O.A.S.T. experiment: Acoustic sounder measurement. *Bound.-Layer Meteor.,* **44,** 359–371.